Anomalous localization and transport behavior of amplifying periodic-on-average random systems at critical disorder

Krishna Joshi,[*] Randhir Kumar,[*] and Sushil Mujumdar[†]

Nano-optics and Mesoscopic Optics Laboratory, Tata Institute of Fundamental Research, 1 Homi Bhabha Road, Mumbai 400005, India

(Received 5 August 2021; accepted 8 February 2022; published 4 March 2022)

Optical amplification in a disordered system leads to modification of the localization properties and the relative fluctuations of transport parameters. Here, we study the effect of gain on the localization properties and transport parameters of Anderson-localized modes at critical disorder in a one-dimensional periodic-on-average random amplifying system. We experimentally measured the inverse participation ratio (IPR) and localization length ξ to quantify the localization behavior. At high disorder, IPR and ξ^{-1} exhibit a linear relationship, as expected from theoretical studies. However, it shows an anomalous behavior below a critical disorder and transitions into a near-quadratic relationship at weak disorder. We further study the mesoscopic conductance g' and statistical distributions of modal and integrated intensities to quantify the transport. The intensity distributions show power-law tails whose exponents show atypical gain dependence across the critical disorder. Motivated by the experimental results, we performed numerical studies using a model based on transfer matrices and laser rate equations which endorses our experimental observations.

DOI: 10.1103/PhysRevA.105.033505

I. INTRODUCTION

Conductive or localized transport of photons in disordered media is a manifestation of wave interference [1]. In a strongly scattering medium, transport is suppressed via multiple scattering and leads to formation of spatially localized resonances called Anderson-localized (AL) modes [2–7]. Introduction of optical gain to the system in the presence of disorder-induced feedback results in the realization of so-called random lasers [8–15]. In a localizing system, resonant AL modes provide the necessary feedback to realize lasing in random cavities, creating an exciting subset of random lasers [16–21]. Lasing over Anderson-localized modes in periodic-on-average (PARS) systems allows us to study the interplay between disorder and gain [22–24]. In one-dimensional (1D) PARS systems, the erstwhile band gap of the periodic system vanishes above certain disorder, called critical disorder δ_{cr} [25–27]. The behavior of AL random lasers shows an interesting transition across δ_{cr} [27].

The localization property of AL random lasers is characterized by the inverse-participation ratio (IPR) and the localization length ξ. IPR is defined as the second moment of the spatial intensity distribution of the eigenfunctions [28,29]. In a completely Anderson localizing system (very high disorder), IPR and ξ are related by the relation IPR $\propto \xi^{-d}$, where d is the dimension of space [30,31]. However, there have not been any reports on the relation between IPR and ξ in the vicinity of δ_{cr} or in the weak-disorder regime. Apart from IPR and ξ, the fluctuations in the relative intensity of the eigenfunctions help to characterize the nature of transport in Anderson-localized systems [17,32–35]. The variance of these fluctuations defines a dimensionless conductance $g' = 2/3\text{var}(s_a)$, where $s_a = I/\langle I\rangle$ is the normalized mode intensity [35–38]. Anderson localization is achieved when $\langle g'\rangle < 1$. In addition to $\langle g'\rangle$, the behavior of the full distribution of mode intensities $P(I/\bar{I})$ has been theoretically reported in random-lasing systems [32,34]. The theoretically predicted distributions for internal and output intensities of lasing modes in a 1D random laser show power-law tails with different exponents [34]. Experimental studies so far have focused on only amplifying systems at high disorder strengths. The fluctuations are expected to show an interesting transitional behavior in the vicinity of critical disorder. Here, we study the fluctuations as a function of gain in different disorder regimes across δ_{cr}. We use 1D arrays of amplifying microdroplets as a model system to study the localization properties and fluctuations in the transport parameters of 1D AL lasers. Over a large ensemble of eigenfunctions, we extract $\langle$IPR$\rangle$ and $\langle\xi^{-1}\rangle$, which exhibit the anticipated linear dependence above δ_{cr} but tend toward a hitherto unpredicted quadratic behavior below δ_{cr}. We measure statistical distributions of modal and integrated intensity and calculate the dimensionless conductance g' therefrom. The power-law exponents of the two distributions and also g' show anomalous gain dependence across δ_{cr}. Our experimental results are followed and corroborated by computational studies using a numerical model based on the transfer-matrix method and laser rate equations.

Figure 1 shows the measurement scheme and the sensitivity of the measurement of lasing-mode profiles. Figure 1(a) shows a representative CCD image of a one-dimensional microdroplet array, made from a 50:50 mixture of methanol and ethylene glycol with an effective refractive index of 1.38. Complete technical details of the formation of the array are given in Ref. [21] and also in Appendix A. Gain is

[*]These authors contributed equally to this work.
[†]mujumdar@tifr.res.in; http://www.tifr.res.in/~nomol

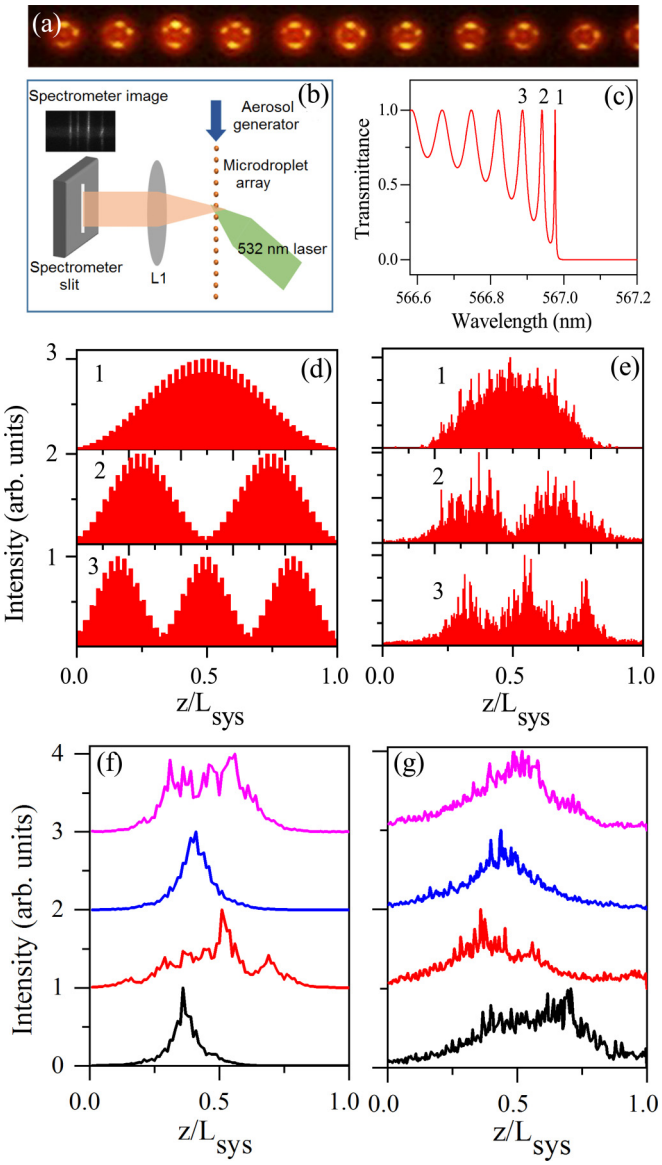

FIG. 1. Experimental measurements. (a) A small portion of the one-dimensional lattice array made of spherical microresonators. (b) Schematic of the experimental setup. (c) Computed transmission spectrum of a passive periodic structure, with peaks enumerating the band-edge modes. (d) Corresponding computed passive-mode profiles of the first three band-edge modes. (e) Experimental lasing-mode profiles of the first three band-edge modes. Four characteristic lasing modes in the localized domain: (f) simulated and (g) experimental.

introduced by adding Rhodamine 6G (0.5 mM). The disorder δ is quantified by using the size measurements made from their whispering-gallery modes and is defined as

$$\delta = n_A\sigma + n_B\sigma,$$

where the refractive indices of the air gap and microresonator are $n_A = 1.0$ and $n_B = 1.4$ respectively, and σ is the standard deviation in the size distribution of micro-resonators.

In our system, δ can be systematically varied in a controlled manner from a few nanometers to a few hundred nanometers. The schematic of the excitation and emission geometry from the array is shown in Fig. 1(b). The array with 60 unit cells is illuminated by a nanosecond pulsed laser (pump) at $\lambda = 532$ nm with a repetition rate of 2 Hz, which excites Anderson-localized lasing modes longitudinally along the array. The spectrally resolved spatial intensity distribution of the Anderson-localized modes is measured in the transverse direction via a spectrometer coupled with an intensified CCD. This provides a direct measurement of spatial eigenmodes.

We model our system as a 1D multilayer with gain. The justification for a 1D approximation is given in Appendix B. Briefly, the excited lasing modes are the collective longitudinal modes of the array. Due to large Dn_B/λ (where $D = 15\ \mu$m is the diameter and $\lambda = 560$ nm), light sees the droplets as quasiplanar layers. Photons scattered in the transverse direction do not experience any feedback and hence do not participate in the formation of any nonlongitudinal collective modes. In our model, we first compute the spatial-mode profiles of the 1D passive multilayer using transfer-matrix simulations. Thereafter, we employ coupled emitter-cavity rate equations to simulate gain [21,23,39]. See Appendix C for details of the theoretical model. The model yields the spatial profile and spectral position of the lasing modes.

To characterize the control and measurement sensitivity of our system, we set out to measure the band-edge lasing modes. The band-edge modes exhibit their squared-sinusoidal intensity profiles only in periodic or very close to periodic arrays. At even smaller disorders, the modes begin to exhibit asymptotic exponential tails. Figure 1(c) shows the computed transmission spectrum of a periodic multilayer (60 unit cells), enumerating first three band-edge modes. Figure 1(d) represents the computed passive spatial-mode profiles with the number of intensity maxima equaling the mode number, where z represents the spatial coordinate and $L_{\rm sys}$ is total length of the system along the longitudinal direction of the array. Figure 1(e) shows the experimentally measured spatial profiles of the first three band-edge lasing modes, in excellent agreement with the computed profiles. The slight exponential tail in the experimental modes arises from very small inherent disorder. This illustrates the fine control in the system. For the subsequent measurements of localized modes, we increase the degree of disorder by moving away from the optimized operating conditions of the array generator. Figures 1(f) and 1(g) represent computed and experimental lasing-mode profiles, respectively, in the localized domain. These modes show high diversity in terms of localizing parameters such as localization length, peakedness, etc. The modes also show a strong variation in their spatial profiles.

Subsequently, we describe the critical disorder $\delta_{\rm cr}$ [25] and study the localization behavior with respect to $\delta_{\rm cr}$. The critical disorder demarcates two regimes of weak disorder below and above which transport parameters vary differently in the passband and band gap. One acknowledged signature of criticality is the crossing of the profiles of mean transmittance and variance of transmittance as a function of disorder [25]. Therefore, we compute the transmission of weakly disordered arrays of passive cavities using the transfer-matrix simulations, with parameters being the same as in experiments. Figure 2(a) represents the average transmittance $\langle T \rangle$ and its variance at the center of the band gap versus disorder strength δ over an ensemble of 4000 configurations. In this case, the

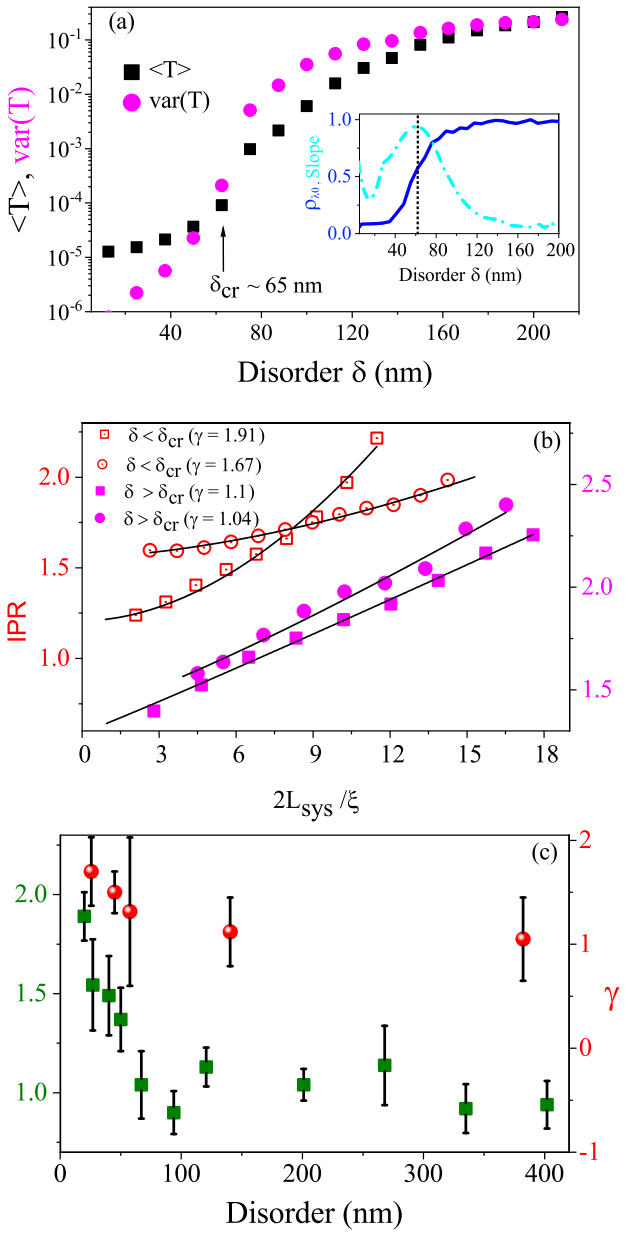

FIG. 2. (a) Computed mean transmittance (black rectangles) and its variance (pink solid circles) over 4000 samples as a function of disorder δ in logarithmic scale. Critical disorder was measured at $\delta_{cr} = 65$ nm. Inset: Mean density of states ρ (blue solid line) and its slope (cyan dotted line) at the center of the photonic band gap ($\lambda_0 = 559.3$ nm) as a function of degree of disorder. (b) Mean IPR vs inverse localization length ($2L_{sys}/\xi$): experimental (circles) and computed (squares) for low (red, empty) and high (magenta , solid) disorders. Black curves represent fit to the function $y = Ax^{\gamma}$. (c) Experimental (red circles, right y axis) and computationally (green squares, left y axis) calculated values of γ as a function of disorder.

critical disorder, $\delta_{cr} = 65$ nm, was found at the crossing of the two curves, as illustrated by the arrow. Above δ_{cr}, the system makes a transition to a regime where fluctuations in the transmission become larger than their mean values [25–27]. We can also define δ_{cr} in terms of the photonic band gap (PBG). Near δ_{cr}, the density of states ρ at the center of the erstwhile PBG ($\lambda_0 = 559.3$ nm) tends to zero as δ decreases. The inset in Fig. 2(a) shows $\rho_{\lambda 0}$ as a function of δ. $\rho_{\lambda 0}$ shows a transition towards zero about the critical disorder $\delta_{cr} = 65$ nm. We identified the transition point by the extremum of the slope of ρ, as shown by the dotted vertical line.

Having established the measurements and critical disorder δ_{cr}, we set out to study the property of the individual modes. In this regard, we study the normalized localization length ($\xi/2L_{sys}$) and the IPR. IPR is given by the relation $\text{IPR} = N\frac{\sum_{i=1}^{N} I_i^2}{(\sum_{i=1}^{N} I_i)^2}$, where I_i is the intensity of the mode at the ith spatial point and N is the total number of spatial points. An IPR value of 1 means a completely delocalized mode, whereas a value of N means a maximally localized mode. ξ is measured from the fit to the exponentially decaying tail of the mode (for details see Appendix D).

Figure 2(b) shows the experimental and computational plots of mean IPR vs $2L_{sys}/\xi$ at two different disorder strengths of 20 and ~300 nm (scatterplots of IPR vs $2L_{sys}/\xi$ of individual modes are shown in Appendix E). The circles show the experimental results, with red (empty) and magenta (filled) circles corresponding to $\delta = 20$ nm and $\delta = 300$ nm, respectively. Similarly, the squares show the computed results, with red (empty) and magenta (filled) squares corresponding to $\delta = 20$ nm and $\delta = 300$ nm, respectively. The black curve in each case is a fit to the function $y = Ax^{\gamma}$. In Anderson-localized systems, in a d-dimensional space, IPR $\propto \xi^{-d}$ [30,31]. Thus, in one dimension, IPR $\propto \xi^{-1}$. Figure 2(c) shows the variation of γ with the degree of disorder δ. The error bars are fit errors to the data. In both the experiment and computation, we get $\gamma \sim 1$ at higher disorder, i.e., $\delta \geqslant 100$ nm. However, at lower disorder, γ is much higher than 1. In the experiment (red solid sphere), $\gamma = 1.7$ at $\delta = 20$ nm, which then decreases with an increase in δ and saturates to a value of approximately 1 at high disorders. The computed γ (green squares) also shows a value of 1.91 at $\delta = 20$ nm and decreases with increasing δ and then saturates to a value $\gamma \approx 1$.

Next, we study the generalized conductance g' which quantifies transport within the system. g' is measured from the spatial-mode intensity values as discussed earlier. Figure 3(a) depicts the measured g' as a function of pump power at three disorder strengths, $\delta = 45$ nm (red squares), 60 nm (blue triangles), and 160 nm (green solid circles). Lines are guides to the eye. The measured g' value is found to decrease monotonically with excitation power at high disorder and drops below 1.0 at 1 mW. At low disorder (red squares), g' initially increases with power and saturates at high power. At the intermediate disorder (blue triangles) g' fluctuates between 1.0 and 1.1. We note that, at high pump power, g' tends to saturate; however, the output intensity I_{out} does not show any saturation with the pump (see Appendix F), which means that these observations are not related to the gain saturation.

In order to further corroborate the experimental results, we performed computational studies as discussed earlier. The time evolution of spatial-mode profiles with the variation of the excitation pump rate R_p is measured by solving the coupled emitter-cavity rate equations and then is averaged over time to get the final effective mode profiles. The computation was performed over 1000 configurations. Figure 3(b) shows the computed g' versus pumping rate R_p for four levels

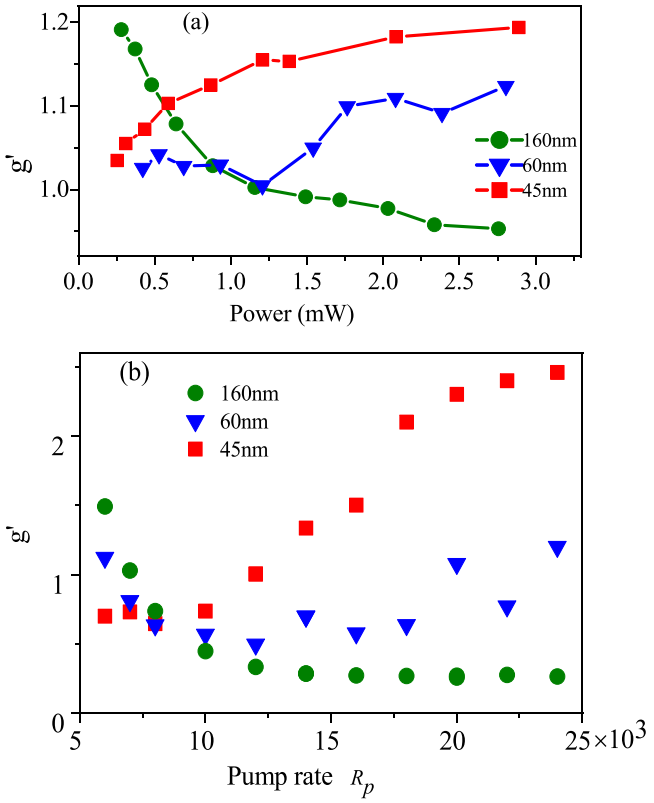

FIG. 3. (a) Experimental and (b) computational measured generalized conductance g' as a function of pump power at three different disorder strengths: $\delta = 45$ nm (red squares), 60 nm (blue triangles), and 160 nm (green solid circles).

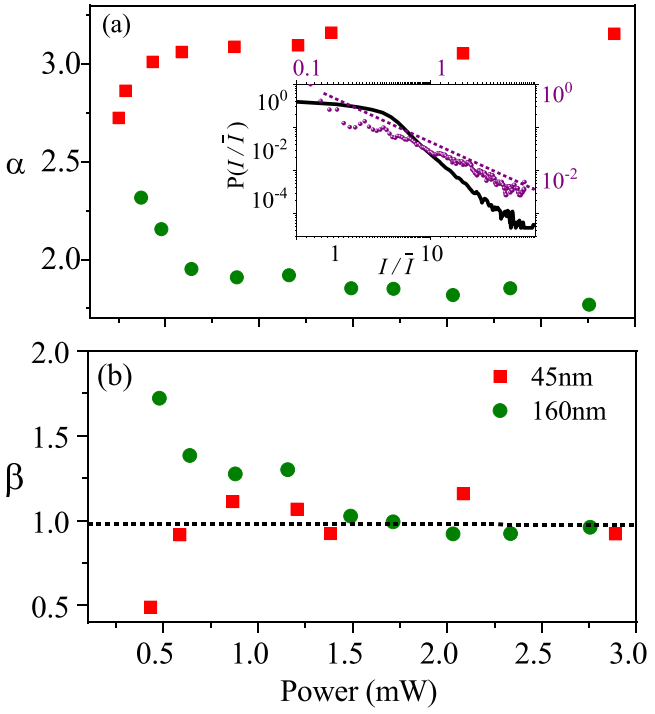

FIG. 4. The inset in (a) shows the probability distribution $P(I/\bar{I})$ of spatial-mode intensities (black line) and integrated mode intensities (purple solid spheres) in log-log scale. The purple dashed line is a power-law fit to the tail of the distribution $P(x) = Ax^{-\alpha}$, $x = I/\bar{I}$ (offset for better visibility). The main plots in (a) and (b) show α and β calculated from the power-law fit as a function of pump power at disorders of 45 nm (red squares) and 160 nm (green solid circles), respectively.

of disorder strengths, $\delta = 45$ nm (red squares), 60 nm (blue triangles), and 160 nm (green solid circles). The computational results agree with the prior experimental results. One feature noted from the above experimental [Fig. 3(a)] and computational [Fig. 3(b)] results is that, as we approach the high disorder values, g' tends to decrease monotonically with pump power, which does not happen at lower disorder. The continuous monotonic decrease in g' values with pump power is obtained as disorder becomes larger than the critical value ($\delta > \delta_{cr}$).

The statistics of lasing intensity shed further light on the transport behavior. As we have seen, depending upon the relative disorder strength with respect to δ_{cr}, the addition of gain to such a system modifies the confinement of light. We further investigated the effect of gain on Anderson localization using two kinds of intensity distributions, namely, the modal intensity distribution $P(I/\bar{I})$ and total integrated intensity distribution $P(I_{tot}/\bar{I}_{tot})$. The modal intensity I is defined as the intensity at each spatial point of the mode, and the distribution $P(I/\bar{I})$ is obtained by combining the modal intensity from a large ensemble of modes. The integrated intensity I_{tot} of a mode is obtained by summing the intensity at each spatial point of the mode, and the distribution $P(I_{tot}/\bar{I}_{tot})$ is obtained by collecting these values from a large ensemble of modes. About 2000 experimentally measured modes were used to obtain the distribution. Both the distributions are normalized by their own ensemble average.

Next, we discuss the statistical behavior of modal intensity and the total integrated intensity. The inset in Fig. 4(a) represents the distributions on logarithmic scales. Both distributions exhibit power-law asymptotic behavior in the tail, an observation that is in excellent agreement with existing theory [34]. As an illustration, the power-law fit to the tail of the total integrated intensity distribution is shown by the purple dotted line (offset from the data for better visibility). We fit the function $Ax^{-\text{exponent}}$ to the tail of the distributions at different pump powers, with α and β being labels for the modal intensity distribution and the integrated intensity distribution, respectively. The value of the exponent quantifies the fluctuations in the distributions. A small exponent indicates a long tail and hence strong fluctuations and vice versa. Figure 4(a) shows α as a function of pump power for two representative disorder strengths, one below δ_{cr} at 45 nm (red rectangles) and another above δ_{cr} at 160 nm (green solid circles). For $\delta = 45$ nm $< \delta_{cr}$, α increases with the increase in pump power and saturates to a value of 3.0 at high pump powers. On the other hand, for $\delta = 160$ nm $> \delta_{cr}$, α decreases with the increase in pump power and saturates to a value of 1.9 at high pump powers. Next, in Fig. 4(b) we plot β as a function of pump power for the same two disorder strengths. Interestingly, β also shows the same distinction in the pump-power dependence with respect to δ_{cr}, although the form of the dependence is reversed. β decreases (increases)

with increasing pump power for disorders below (above) δ_{cr} and saturates to $\beta = 1$ at high pump powers. Our experimental results are also corroborated by the computations. The computed results are shown in Appendix G. We therefore observe that the pump-power dependence of the intensity distributions exhibits opposite behaviors in two different disorder regimes with respect to δ_{cr}. This directly traces out the anomalous transport behavior in our system at the critical disorder.

In summary, we have studied the effect of amplification on the localization properties and fluctuations in the transport parameters of a 1D Anderson-localizing system in different disorder regimes both experimentally and numerically. IPR and ξ^{-1} show a linear interdependence at high disorders, as expected; however, the relationship tends to quadratic below critical disorder. Mesoscopic conductance g' and the statistics of modal and integrated intensity were measured to quantify transport behavior. The modal and integrated intensity distributions show power-law tails, with exponents α and β, respectively. g', α, and β show anomalous excitation power dependence across the critical disorder δ_{cr}. We followed the experimental investigations by numerical studies using a model based on the transfer-matrix method and coupled emitter-cavity equations which corroborate the experimental findings. Our results thus unveil the anomalous statistical behavior of a 1D Anderson-localizing system in the presence of gain across δ_{cr}.

These studies reveal the rich physics of Anderson-localizing systems and the consequences introduced by the realization of amplification therein. Importantly, the data bring out the intricacies of Anderson localization at weak disorder. As discussed in the seminal theoretical works [40], this regime relies on the delicate interplay of order and disorder due to which the reinterpreted Ioffe-Regel criterion essentially incorporates the inverse of the fluctuation in the wave vector from the Bragg plane. The resulting macroscopic resonances play the role of lasing cavities in the presence of gain, manifesting a synergy between coherent amplification and wave confinement [19]. As seen from our results, this synergy leads to unexpected behavior in Anderson-localization-based lasers.

ACKNOWLEDGMENTS

We would like to acknowledge the Swarnajayanti Fellowship from the Department of Science and Technology, Government of India. We acknowledge funding from the Department of Atomic Energy, Government of India (Grant No. 12-R & D-TFR-5.02-0200).

APPENDIX A: METHOD OF GENERATING THE MICRO-RESONATOR ARRAY

A one-dimensional array of microresonators (CCD image) is generated using a microcapillary tube, which is based on the vibrating-orifice aerosol-generator technique. The orifice diameter (output end) of the capillary is about 10 μm. It is connected to a piezoelectric gate coupled with a signal generator which creates perturbation via vibration in the orifice, as shown in the Fig. 5. The liquid chamber is filled with a solution made of methanol, ethylene glycol, and Rhodamine 6G dye (gain). The solution inside the chamber is forced through the orifice, which results in the formation of cylindrical jets. Under the appropriate periodic perturbation (amplitude, frequency, etc., of the signal from the signal generator), the jet breaks up into periodically placed homogeneous droplets. The diameter of the droplets is measured using their Mie modes, called whispering-gallery modes. Disorder is introduced in the array by slightly changing the perturbation frequency from the prescribed frequency, which results in the formation of a nonhomogeneous array of microresonators.

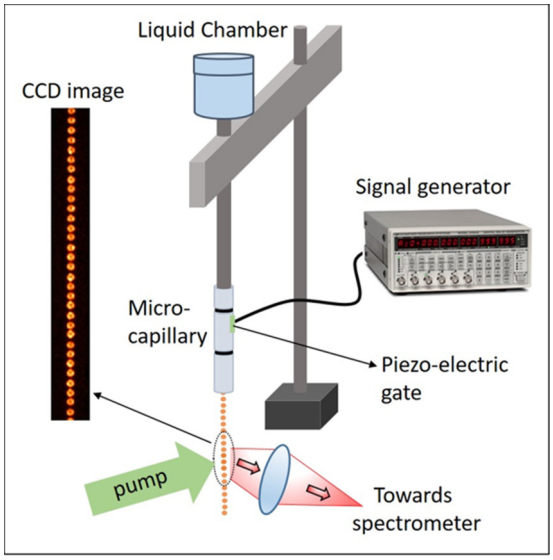

FIG. 5. Schematic explaining the formation of the array.

APPENDIX B: JUSTIFICATION OF THE 1D APPROXIMATION OF OUR SYSTEM

Our system is essentially a 1D linear chain of cavities. However, given that the diameters of the cavities are of the order of 15 μm, the curvatures of the spherical surfaces are rather large compared to the wavelength. To be precise, $\lambda \sim 560$ nm, $n_{\text{eff}} = 1.38$, and diameter $D \sim 15$ μm, so $Dn_{\text{eff}}/\lambda \sim 37$. Thus, effectively, the light sees quasiplanar layers that realize the multiple reflections.

Next, given the linear configuration, the periodicity exists only in the Z direction. Hence, the mode is set up only along the longitude of the array. The slight curvature of the interfaces (slight because $D \sim 37\lambda$) of the spherical resonators results in scattering of the mode into the space outside. This light does not reenter the system as there are no scatterers to feed this light back from outside of the chain. The intensity

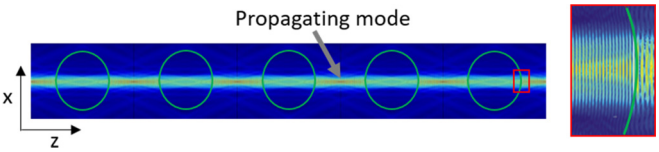

FIG. 6. Intensity distribution of the mode showing one-dimensional propagation.

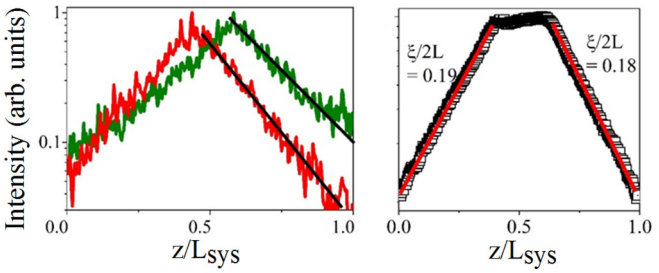

FIG. 7. Spatial intensity profiles in semilogarithmic scale. Left: Two representative mode profiles with an exponentially decaying fit (black lines). Right: Averaged mode profile over 1000 samples. Each mode profile is fitted with an exponential decay function $e^{-2z/\xi}$, where ξ is the localization length (decay length).

distribution of the longitudinal mode is shown in Fig. 6. This is calculated from a finite-element computation. The intensity distribution clearly shows that the mode propagating in one dimension has almost planar wave fronts. The transverse extent of the mode is much narrower than D, as seen in Fig. 6, and hence can be considered to be reflected off the planar interfaces. The red rectangle is emphasized, showing the near-planar wave fronts of light, endorsing the 1D multilayer approximation.

APPENDIX C: THEORETICAL MODEL

In order to model the time-dependent gain process under pulse excitation, we employ coupled emitter-cavity rate equations based on two level lasers [21,23,39]. Our model is a 1D bilayer system which is discretized into multiple spatial points. At each spatial point, the time evolution of the photon numbers is described by two coupled rate equations:

$$\frac{dn_{ij}}{dt} = K_{ij}N_{2,j}(n_{ij}+1) - \gamma_{c,i}n_{ij}, \tag{C1}$$

$$\frac{dN_{2,j}}{dt} = R_p - \sum_i K_{ij}N_{2,j}n_{ij} - \gamma_2 N_{2,j}. \tag{C2}$$

Here, n_{ij} is the photon number in the ith mode at the spatial location j of the cavity, which has a decay rate of $\gamma_{c,i}$. $N_{2,j}$ is the upper-level population at the same position, R_p is the pumping rate, and γ_2 is the spontaneous decay rate to lower levels. K_{ij} is the coupling coefficient between the emitter and the ith mode at position j. The final output intensity in the ith mode is given by $n_{\text{out},i} = \sum_j \gamma_{c,i}n_{ij}$. The cavity parameters

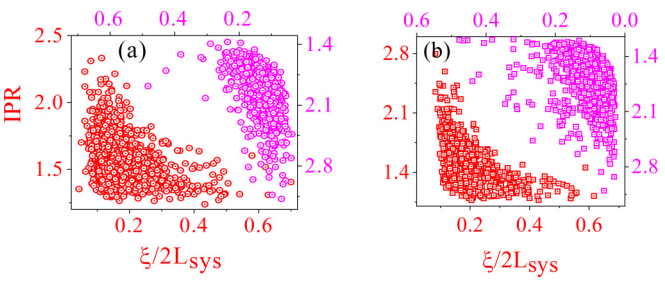

FIG. 8. Scatterplots of IPR vs localization length at weak (red) and high (pink) disorders: (a) experimental and (b) simulated results.

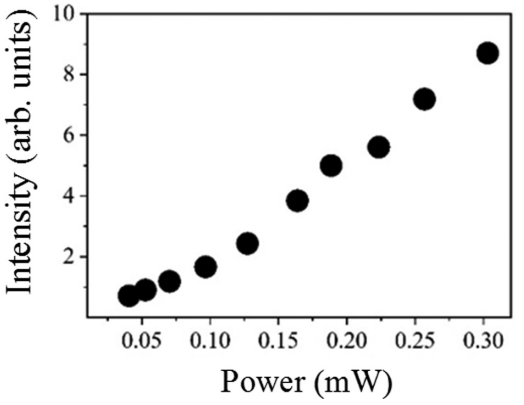

FIG. 9. Lasing output intensity I_{out} from the coupled microresonator array as a function of input pump power.

required in the model are computed from the transfer-matrix method for a dielectric-air bilayer, which is a common technique for one-dimensional systems.

APPENDIX D: MEASUREMENT OF THE LOCALIZATION LENGTH

We measured the localization length (spatial extent) ξ by imaging the spatial intensity distribution of the mode. Figure 7 shows spatial-mode profiles in semilogarithmic scale. The left and right panels represent two individual and ensemble-averaged mode profiles, respectively. The profiles clearly exhibit a tight exponential decay in the wings which is used to characterize ξ. In order to calculate ξ, each wing of the mode (either right or left) is fitted with an exponentially decaying function $e^{-2z/\xi}$, as shown in Fig. 7. In Fig. 7, we have normalized the spatial dimension z by total system length L. The mean ξ of the system can also be measured from the ensemble-averaged mode profile (right panel), showing

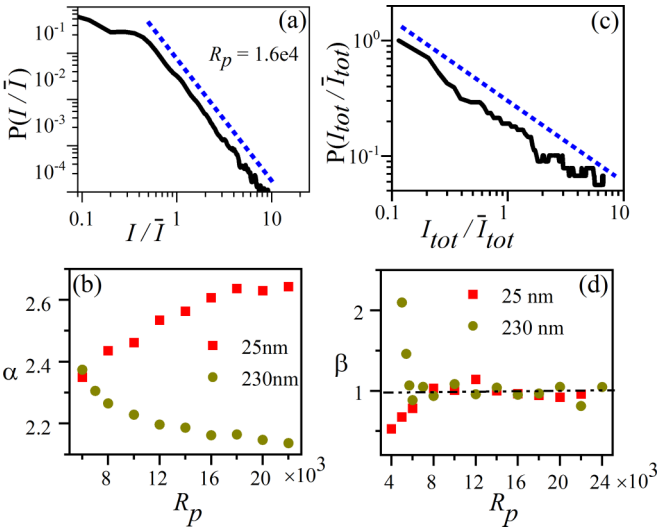

FIG. 10. (a) Distribution $P(I/\bar{I})$ of spatial-mode intensities. (b) Exponent α as a function of pump rate R_p. (c) Distribution $P(I_{\text{tot}}/\bar{I}_{\text{tot}})$ of integrated mode intensities. (d) β vs R_p.

exponential decay on either side. In this case, the measured $\xi/2L$ are 0.19 (left wing) and 0.18 (right wing).

APPENDIX E: IPR VERSUS LOCALIZATION LENGTH

Figure 8 shows the scatterplots of IPR vs ξ of individual modes for the $\delta = 25$ nm (red) and $\delta = 230$ nm (pink) disorders. Figures 8(a) and 8(b) are experimental and computed results, respectively.

APPENDIX F: DEPENDENCE OF LASING-MODE INTENSITY ON PUMP POWER

In order to see the gain-dependence behavior, we looked at the output intensity of the lasing modes. Figure 9 shows the output lasing intensity I_{out} as a function of input pump power. The plot shows an almost linear behavior with pump power.

APPENDIX G: COMPUTED INTENSITY DISTRIBUTIONS $P(I/\bar{I})$ AND EXPONENTS α AND β

Figure 10(a) shows the computed distribution of spatial-mode intensities $P(I/\bar{I})$ in log-log scale. The distribution shows power-law behavior in the tail, as shown by the fit dotted line. The fit distribution function is given by $P(x) = Ax^{-\alpha}$, $x = I/\bar{I}$. Figure 10(b) shows exponent α as a function of pump rate R_p at two disorder values: $\delta = 25$ nm (red rectangles) and $\delta = 230$ nm (dark yellow circles). Figure 10(c) shows the probability distribution $P(I_{\text{tot}}/\bar{I}_{\text{tot}})$ of integrated mode intensities. Again, the distribution shows power-law behavior $P(x) = Ax^{-\beta}$. Exponent β as a function of pump rate R_p is plotted in Fig. 10(d) for two disorder values: $\delta = 25$ nm (red rectangles) and $\delta = 230$ nm (dark yellow circles). All these computational observations show good agreement with our experimental results.

[1] *Scattering and Localization of Classical Waves*, edited by P. Sheng (World Scientific, Singapore, 1990).

[2] P. W. Anderson, Absence of diffusion in certain random lattices, Phys. Rev. **109**, 1492 (1958).

[3] D. S. Wiersma, P. Bartolini, A. Lagendijk, and R. Righini, Localization of light in a disordered medium, Nature (London) **390**, 671 (1997).

[4] Y. Lahini, A. Avidan, F. Pozzi, M. Sorel, R. Morandotti, D. N. Christodoulides and Y. Silberberg, Anderson Localization and Nonlinearity in One-Dimensional Disordered Photonic Lattices, Phys. Rev. Lett. **100**, 013906 (2008).

[5] F. Riboli, P. Barthelemy, S. Vignolini, F. Intonti, A. De Rossi, S. Combrie, and D. S. Wiersma, Anderson localization of near-visible light in two dimensions, Opt. Lett. **36**, 127 (2011).

[6] T. Schwartz, G. Bartal, S. Fishman, and M. Segev, Transport and Anderson localization in disordered two-dimensional photonic lattices, Nature (London) **446**, 52 (2007).

[7] L. Sapienza, H. Thyrrestrup, S. Stobbe, P. D. García, S. Smolka and P. Lodahl, Cavity quantum electrodynamics with Anderson-localized modes, Science **327**, 1352 (2010).

[8] N. M. Lawandy, R. M. Balachandran, A. S. L. Gomes, and E. Sauvain, Laser action in strongly scattering media, Nature (London) **368**, 436 (1994).

[9] D. S. Wiersma, The physics and applications of random lasers, Nat. Phys. **4**, 359 (2008).

[10] R. Pierrat and R. Carminati, Threshold of random lasers in the incoherent transport regime, Phys. Rev. A **76**, 023821 (2007).

[11] A. S. Gomes, E. P. Raposo, A. L. Moura, S. I. Fewo, P. I. Pincheira, V. Jerez, L. J. Maia, and C. B. de Arajo, Observation of Lévy distribution and replica symmetry breaking in random lasers from a single set of measurements, Sci. Rep. **6**, 27987 (2016).

[12] A. S. L. Gomes, B. C. Lima, P. I. R. Pincheira, A. L. Moura, M. Gagn, E. P. Raposo, C. B. de Arajo, and R. Kashyap, Glassy behavior in a one-dimensional continuous-wave erbium-doped random fiber laser, Phys. Rev. A **94**, 011801(R) (2016).

[13] A. S. L. Gomes, A. L. Moura, C. B. de Arajo, and E. P. Raposo, Recent advances and applications of random lasers and random fiber lasers, Prog. Quantum Electron. **78**, 100343 (2021).

[14] S. K. Turitsyn, S. A. Babin, A. E. El-Taher, P. Harper, D. V. Churkin, S. I. Kablukov, J. D. Ania-Castaon, V. Karalekas, and E. V. Podivilov, Random distributed feedback fibre laser, Nat. Photonics **4**, 231 (2010).

[15] S. K. Turitsyn, S. A. Babin, D. V. Churkin, I. D. Vatnik, M. Nikulin, and E. V. Podivilov, Random distributed feedback fibre lasers, Phys. Rep. **542**, 133 (2014).

[16] H. Cao, Y. G. Zhao, S. T. Ho, E. W. Seelig, Q. H. Wang, and R. P. H. Chang, Random Laser Action in Semiconductor Powder, Phys. Rev. Lett. **82**, 2278 (1999).

[17] J. Liu, P. D. Garcia, S. Ek, N. Gregersen, T. Suhr, M. Schubert, J. Mørk, S. Stobbe, and P. Lodahl, Random nanolasing in the Anderson localized regime, Nat. Nanotechnol. **9**, 285 (2014).

[18] V. Milner and A. Z. Genack, Photon Localization Laser: Low-Threshold Lasing in a Random Amplifying Layered Medium via Wave Localization, Phys. Rev. Lett. **94**, 073901 (2005).

[19] P. Pradhan and N. Kumar, Localization of light in coherently amplifying random media, Phys. Rev. B **50**, 9644 (1994).

[20] A. K. Tiwari and S. Mujumdar, Random Lasing over Gap States from a Quasi-One-Dimensional Amplifying Periodic-on-Average Random Superlattice, Phys. Rev. Lett. **111**, 233903 (2013).

[21] R. Kumar, M. Balasubrahmaniyam, K. S. Alee, and S. Mujumdar, Temporal complexity in emission from Anderson localized lasers, Phys. Rev. A **96**, 063816 (2017).

[22] M. Balasubrahmaniyam, K. Joshi, and S. Mujumdar, Strong spectrospatial correlations in Anderson-localized lasing in periodic-on-average random systems, Phys. Rev. A **100**, 033804 (2019).

[23] K. Joshi, S. Mondal, R. Kumar, and S. Mujumdar, Reduction in generalized conductance with increasing gain in amplifying Anderson-localized systems, Opt. Lett. **45**, 2239 (2020).

[24] K. S. Alee, R. Kumar and S. Mujumdar, Weak-disorder-induced reduction of the lasing threshold in periodic systems, Phys. Rev. A **91**, 053818 (2015).

[25] M. A. Kaliteevski, D. M. Beggs, S. Brand, R. A. Abram, and V. V. Nikolaev, Statistics of the eigenmodes and optical properties of one-dimensional disordered photonic crystals, Phys. Rev. E **73**, 056616 (2006).

[26] M. Balasubrahmaniyam and S. Mujumdar, Direct experimental determination of critical disorder in one-dimensional weakly disordered photonic crystals, Phys. Rev. B **98**, 184203 (2018).

[27] K. Joshi, R. Kumar, M. Balasubrahmaniyam, and S. Mujumdar, Effect of critical disorder on lifetime distributions of Anderson-localized lasing modes, Phys. Rev. A **100**, 023803 (2019).

[28] P. Pradhan and S. Sridhar, Correlations due to Localization in Quantum Eigenfunctions of Disordered Microwave Cavities, Phys. Rev. Lett. **85**, 2360 (2000).

[29] P. Pradhan and S. Sridhar, From chaos to disorder: Statistics of the eigenfunctions of microwave cavities, Pramana **58**, 333 (2002).

[30] P. Henseler, Interplay of Anderson localization and strong interactions in disordered systems, Ph.D. thesis, University of Bonn, 2009.

[31] N. Trivedi and D. Heidarian, Can disorder drive a Mott insulator into a metal in 2D? Prog. Theor. Phys. Suppl. **160**, 296 (2005).

[32] A. Yamilov and H. Cao, Effects of localization and amplification on intensity distribution of light transmitted through random media, Phys. Rev. E **70**, 037603 (2004).

[33] A. Yamilov and H. Cao, Effect of amplification on conductance distribution of a disordered waveguide, Phys. Rev. E **74**, 056609 (2006).

[34] O. Zaitsev, L. Deych, and V. Shuvayev, Statistical Properties of One-Dimensional Random Lasers, Phys. Rev. Lett. **102**, 043906 (2009).

[35] S. Smolka, Quantum correlations and light localization in disordered nanophotonic structures, Ph.D. thesis, Technical University of Denmark, 2010.

[36] A. A. Chabanov, M. Stoytchev, and A. Z. Genack, Statistical signatures of photon localization, Nature (London) **404**, 850 (2000).

[37] M. C. W. van Rossum and Th. M. Nieuwenhuizen, Multiple scattering of classical waves: Microscopy, mesoscopy, and diffusion, Rev. Mod. Phys. **71**, 313 (1999).

[38] M. Stoytchev and A. Z. Genack, Measurement of the Probability Distribution of Total Transmission in Random Waveguides, Phys. Rev. Lett. **79**, 309 (1997).

[39] A. E. Siegman, *Lasers* (University Science Books, Mill Valley, CA, 1986).

[40] S. John, Strong Localization of Photons in Certain Disordered Dielectric Superlattices, Phys. Rev. Lett. **58**, 2486 (1987).